A New Model for Nanoscale Enamel Dissolution

Lijun Wang,[†] Ruikang Tang,[†] Tammy Bonstein,[‡] Christine A. Orme,[§] Peter J. Bush,[‡] and George H. Nancollas*,[†]

Department of Chemistry, School of Dental Medicine, University at Buffalo, The State University of New York, Buffalo, New York 14260, and Lawrence Livermore National Laboratory, Livermore, California 94550

Received: August 6, 2004; In Final Form: October 14, 2004

The dissolution kinetics of human tooth enamel surfaces was investigated using nanomolar-sensitive constant composition (CC) and in situ atomic force microscopy (AFM) under simulated caries formation conditions (relative undersaturation with respect to hydroxyapatite = 0.902, pH = 4.5). Scanning electron microscopic (SEM) examination of the resulting etched enamel surfaces showed that deminerzalization, initiated at core/wall interfaces of rods, developed anisotropically along the *c*-axes. After an initial rapid removal of surface polishing artifacts, the dissolution rate decreased as the reaction proceeded in accordance with our recently proposed crystal dissolution model, resulting in hollow enamel cores and nanosized remaining crystallites, resistant to further dissolution. Generally, dissolution of minerals is regarded as a spontaneous reaction in which all the solid phase can be dissolved in undersaturated solutions. However, the dissolution of some biominerals may be suppressed when the crystallites approach nanometer size. This study shows that CC demineralization of enamel in acidic medium follows this new model that can be used to mimic carious lesion formation. In dissolution studies, nanosized enamel crystallites exhibit a remarkable degree of self-preservation in the fluctuating physiological milieu.

I. Introduction

Tooth enamel, the hardest human mineralized tissue, is composed almost exclusively (above 95 wt %) of apatite-like crystallites with highly organized hierarchical structures. Scanning electron microscopy (SEM) of enamel surfaces shows well-organized rodlike structures, with the apatite crystals elongated in their *c*-axis directions, which lie predominantly parallel to the rod axes.[1] Despite these complex hierarchical structures, the basic building blocks for mineralized tissues are of nanoscale dimensions. In the process of enamel crystal formation, thin ribbonlike crystals that initially deposit in the enamel matrix eventually grow into flat hexagonal prisms.[2] High-resolution transmission electron microscopy (TEM) has revealed the role of nanometer-sized particles which serve as precursors in the formation of the elongated ribbonlike crystals.[3,4]

Amelogenin proteins constitute the primary structural entity of the extracellular protein framework of the developing enamel matrix. Recent data show that the dominant protein of enamel, amelogenin, self-assembles by protein-to-protein interactions to form nanospheres (18−20 nm diameter).[5,6] Hydrophobic nanospheres further assemble to form larger nanospheres with diameters of 20−200 nm, thereby stabilizing the matrix containing the initial enamel crystallites.[7] Nanospheres can interact with specific surfaces of growing hydroxyapatite crystallites and limit crystal growth to certain kinetically preferred orientations.[8−10] Following secretion, the amelogenins undergo a proteolytic degradation,[11] and crystallites thicken and eventually may fuse

to generate the mature enamel. Previous studies and our current results of in situ electron dispersive spectroscopy (EDS), X-ray diffraction (XRD), X-ray photoelectron spectroscopy (XPS), and infrared (IR) indicate identical chemical and crystallographic properties of the minerals in the cores and on the walls of enamel rods after complete maturation.[12]

Gao et al. have shown that the size of the mineral particles (typically tens to hundreds of nanometers) is not arbitrary.[13] Rather, it seems to give biominerals such as bone and tooth remarkable characteristics: As the mineral size falls below a critical length scale (around 30 nm), the strength of a perfect mineral crystal is maintained despite defects. It seems clear that the weakening effect of structural flaws vanishes specifically at the nanoscale.[13] Recent dissolution studies of synthetic enamel-like hydroxyapatite have revealed an interesting and unusual behavior in that dissolution rates decreased, eventually resulting in effective suppression, when their sizes fell into a critical length scale, always at the nanoscale.[14,15] The important questions are why the nanoscale is so important for biomaterials and how this phenomenon of self-inhibiting dissolution can be modeled. In this paper, we combine experimental observations of enamel dissolution kinetics and propose a model for nanoscale enamel dissolution.

II. Materials and Methods

Twenty freshly extracted caries-free and filling-free human molars, stored for less than two weeks in 0.5% Chloramine-T, were used in this study. Each tooth was cut horizontally at the cemento enamel junction (CEJ) to remove the root portion. The crown was cut vertically (parallel to the tooth axis). Vertical cuts from the buccal and lingual sides of the crown produced two enamel disks about 2 mm thick from each tooth (40 disks in all). All disks were made using a slow-speed diamond saw (Buehler Isomet 1000 precision saw) with water irrigation.

* Corresponding author: Prof. George H. Nancollas, 756 Natural Sciences Complex, University at Buffalo, The State University of New York, Buffalo, NY 14260 U.S.A. Email: ghn@buffalo.edu. Phone: +1-716-645-6800 ext. 2210. Fax: +1−716-645-6947.
† Department of Chemistry.
‡ School of Dental Medicine.
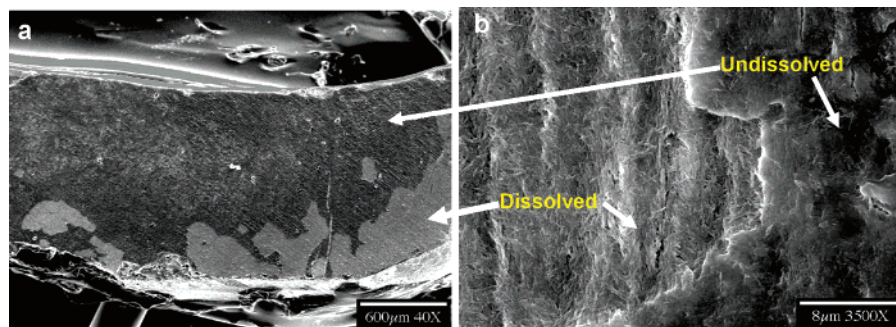§ Lawrence Livermore National Laboratory.

Figure 1. Scanning electron micrographs of the polished layer at an enamel surface (parallel to the rod c-axis) after 200 min of dissolution (pH = 4.5, I = 0.15 mol L^{-1}, 37 °C at σ = 0.902). (a) Lower magnification. (b) Higher magnification.

Samples were cleaned by ultrasonication in distilled water for 5 min before and after polishing and were serially polished using progressively finer silicon carbide papers (P800, P1000, P1200, P2400, and P4000) (Struers, Denmark). The samples were polished either parallel or perpendicular to the enamel rod c-axis and were rinsed and sonicated in deionized water after each polishing step to remove any debris. An acid-resistant varnish was applied to some samples, leaving a window exposed to the environment on the outer surface of the enamel disk. Nylon fishing line was affixed by nail varnish to the opposing unexposed surface of each disk, so that it could be suspended in the reaction solution. The disks were then washed by ultrasonication in distilled water in order to ensure the removal of any residual contaminants.

In the constant composition (CC) method, multiple titrant solutions were added simultaneously to the reaction solutions to compensate for changes of lattice ion concentrations during the reactions.[16] Titrants were prepared having stoichiometries matching those of the dissolving phases while taking into account dilution effects.

The CC curves were recorded as plots of added titrant volume, V, against time, t, and the dissolution rates were calculated from their slopes, dV/dt, by eq 1

$$R = (C_{eff}/A_T) \cdot (dV/dt) \quad (1)$$

where the bulk dissolution rate, R, is expressed as equivalent moles of hydroxyapatite dissolved per mm^2 of surface per min. C_{eff} is the effective titrant concentration (i.e., the moles of dissolved crystallites per liter of added titrant). A_T is the enamel surface area measured by light microscopy.

The dissolution experiments, initiated by the introduction of known amounts of enamel sample, were conducted in magnetically stirred (450 rpm) double-walled Pyrex vessels thermostated at 37.0 ± 0.1 °C. Nitrogen, saturated with water vapor at 37 °C, was purged through the reaction solutions to exclude carbon dioxide. The ionic strength was adjusted to 0.15 mol L^{-1} using NaCl solutions. Reaction solutions were adjusted to pH = 4.50 by the dropwise addition of HCl (0.05 mol L^{-1}).

The relative undersaturation is defined by eq 2

$$\sigma = 1 - S \quad (2)$$

and

$$S = \left[\frac{(Ca^{2+})^{10}(PO_4^{3-})^6(OH^-)^2}{K_{sp}} \right]^{1/18} \quad (3)$$

where K_{sp} is the thermodynamic solubility product and the brackets represent ionic activities. A σ value of 0.902 was achieved using total molar concentrations: calcium, T_{Ca} = 1.00
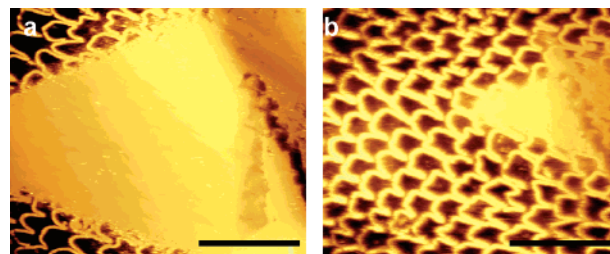

Figure 2. AFM images of the dissolution of a polished layer at an enamel surface (perpendicular to the rod c-axis) (a) initially and (b) after 1 h dissolution. Scale bars, 30 μm.

× 10^{-3} mol L^{-1}, and phosphate, T_P = 6.00 × 10^{-4} mol L^{-1}, with C_{eff} = 1.00 × 10^{-4} mol L^{-1}.

Titrant addition was triggered by a potentiometer (Orion 720A, U.K.) incorporating glass (Orion No. 91-01, U.K.) and reference Ag/AgCl (Orion 900100, U.K.) electrodes. During the dissolution, the potential of the potentiometer was constantly compared with a preset value, and the difference, or error signal, activated motor-driven titrant burets, thereby maintaining a constant thermodynamic dissolution driving force. During the reactions, samples were periodically withdrawn, and the solutions were analyzed for total calcium (atomic absorption) and phosphate (spectrophotometrically as the vanadomolybdate complex). During the experiments, concentrations remained constant to ±1%.

Crystallites for SEM investigation (Hitachi S-4000 FESEM) were separated from the bulk solution by filtration (Nuclepore N003 filter membrane, 30 nm pore size) at the end of the dissolution experiment and were dried at room temperature. After coating with 20 nm of evaporated carbon, secondary electron images were collected using a primary beam voltage at 20 keV.

A continuous-flow, single-pass wet atomic force microscope (AFM with a Nanoscope III controller) was used for the in situ dissolution investigations. Ion speciation of the flowing solutions was identical to those of the reaction solutions in CC experiments. The AFM was operated in contact mode using uncoated silicon cantilevers, and the images were recorded continuously.

III. Results and Discussion

Upon introduction into the undersaturated solutions (pH = 4.5, I = 0.15 mol L^{-1}, 37 °C at σ = 0.902), disturbed outer layers at the enamel surfaces resulting from polishing procedures were removed on faces both parallel (Figure 1) and perpendicular (Figure 2) to the rod c-axis of the polished surface of dental enamel. SEM images of the polished layer at the enamel surface (parallel to the rod c-axis) after 200 min of dissolution show the dissolved regions (lighter areas, Figure 1a). Characteristic rod structures and needlelike apatite crystals were
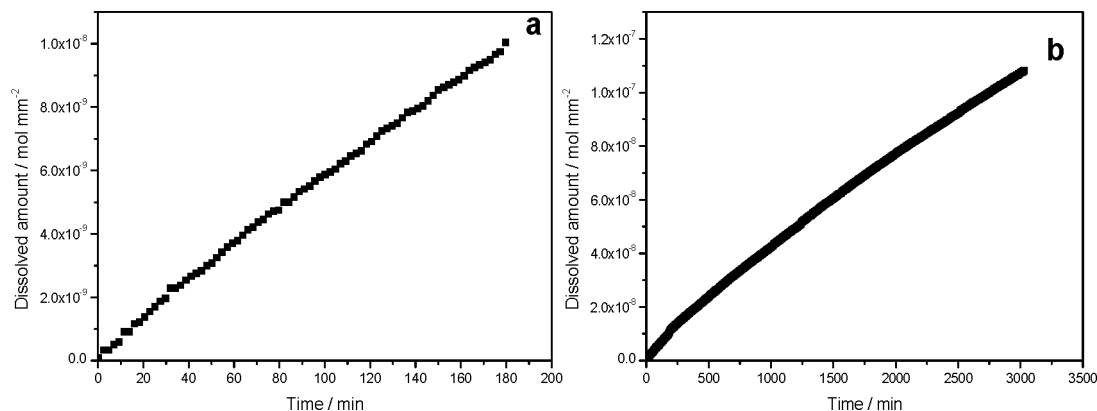
Nanoscale Enamel Dissolution

J. Phys. Chem. B, Vol. 109, No. 2, 2005 **1001**

Figure 3. CC dissolution curves of enamel (one surface exposed to acid, pH = 4.5, I = 0.15 mol L^{-1}, 37 °C) at σ = 0.902. The dissolution rate perpendicular to the rod c-axis of the polished surface decreased as the reaction proceeded from (a) 5.4 ± 0.5 × 10^{-11} mol mm^{-2} min^{-1} after 180 min to (b) 3.5 ± 0.5 × 10^{-11} mol mm^{-2} min^{-1} after 3000 min dissolution.
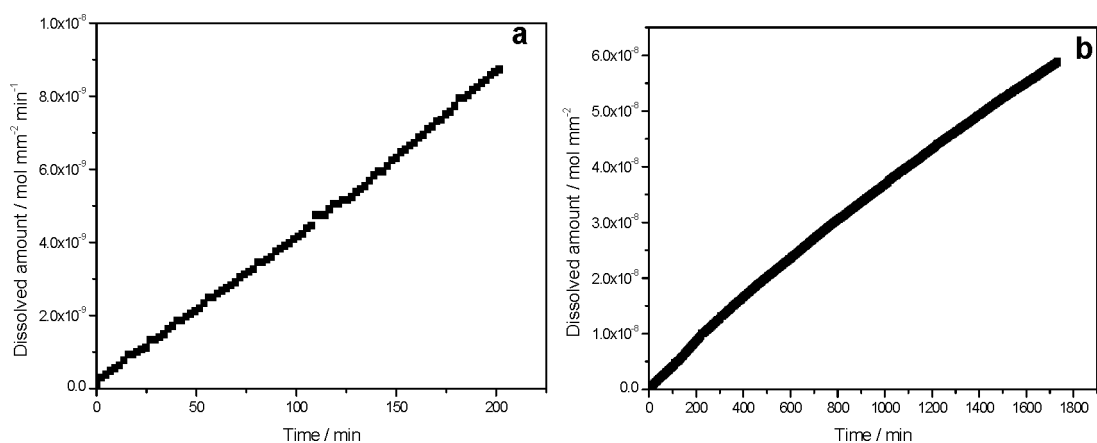

Figure 4. CC dissolution curves of enamel (one surface exposed to acid, pH = 4.5, I = 0.15 mol L^{-1}, σ = 0.902, 37 °C). The dissolution rate parallel to the rod c-axis of the polished surface decreased as the reaction proceeded from (a) 4.2 ± 0.5 × 10^{-11} mol mm^{-2} min^{-1} after 200 min to (b) 3.3 ± 0.5 × 10^{-11} mol mm^{-2} min^{-1} after 1800 min dissolution.

exposed after 2−3 h of dissolution (Figure 1b). AFM images showed that dissolution occurred at the boundary between undissolved and dissolved sections. Prior to the complete dissolution of polishing layers, the characteristic fish-scale "keyhole" structure at the surface was not visible (Figure 2a). After 1 h of dissolution, however, the native enamel surface can be clearly seen (Figure 2b). In the CC experiments, the dissolution rate perpendicular to the rod c-axis decreased as the reaction proceeded from 5.4 ± 0.5 × 10^{-11} mol mm^{-2} min^{-1}, at 180 min reaction (Figure 3a), to 3.5 ± 0.5 × 10^{-11} mol mm^{-2} min^{-1}, at 3000 min dissolution (Figure 3b), and the rate of demineralization parallel to the rod c-axis decreased from 4.2 ± 0.5 × 10^{-11} mol mm^{-2} min^{-1}, at 200 min reaction (Figure 4a), to 3.3 ± 0.5 × 10^{-11} mol mm^{-2} min^{-1}, at 1800 min dissolution (Figure 4b). It can be seen that the polishing treatment increased the dissolution rate of enamel, and the loss of mineral with time during this bulk dissolution was nearly linear for both directions, but the perpendicular rate was, on average, higher than that parallel to the rod c-axis. Using a scanning microradiographic method, Anderson et al. showed that the rates of demineralization of enamel perpendicular and parallel to the natural surface were both approximately constant with time after an initial sigmoidal period of dissolution.[17−20] Chow and Takagi also showed that the rate of demineralization became constant only after 2 days.[21] The initial sigmoidal period may be due to properties of surface enamel different from those of the subsurface regions.

Human enamel is an inhomogeneous tissue with gradients in composition from the natural surface to the enamel−dentin junction (EDJ). The approximate 10% reduction in mineral concentration from the surface to the EDJ is in agreement with that measured in enamel.[22] This anisotropy and inhomogeneity of enamel suggest that the rate of demineralization would depend on the direction and position of the acid attack within a developing lesion.[23] However, the CC results suggest that this factor does not appear to influence the linearity of the mineral loss with time when the enamel surface is demineralized after removal of the polishing layer. The rates of demineralization in directions perpendicular and parallel to the rod c-axis are both approximately constant with time, the former being higher than the latter.

When polishing layers at the surfaces were completely removed, native enamel surfaces were exposed to the solution. SEM results showed that demineralization was initiated at core/wall interfaces of rods and developed anisotropically along c-axes (Figure 5). Apatite crystallites both in the cores and on the walls underwent a similar demineralization process. Figure 6 shows walls and cores at an intermediate stage of the dissolution reaction, in which apatite nanoparticles 100−200 nm in size can be seen on both cores and walls. Using AFM, Farina et al. showed that enamel surfaces after brief acidic treatments were roughened and contained tiny globular particles.[24] However, further dissolution of the nanoparticles was suppressed in our experiments; those from cores were released
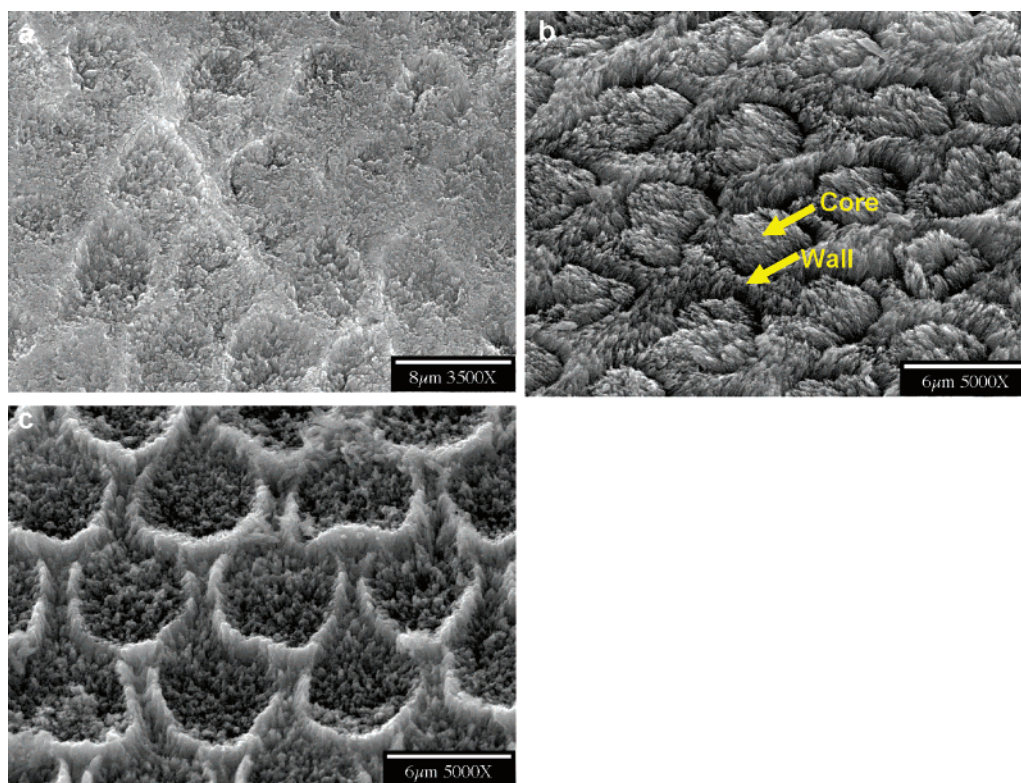
Figure 5. SEMs show that demineralization was initiated at the core/wall interfaces of rods and developed anisotropically along the *c*-axis. (dissolution time: a, 1600 min; b, 2400 min; c, 3300 min.)
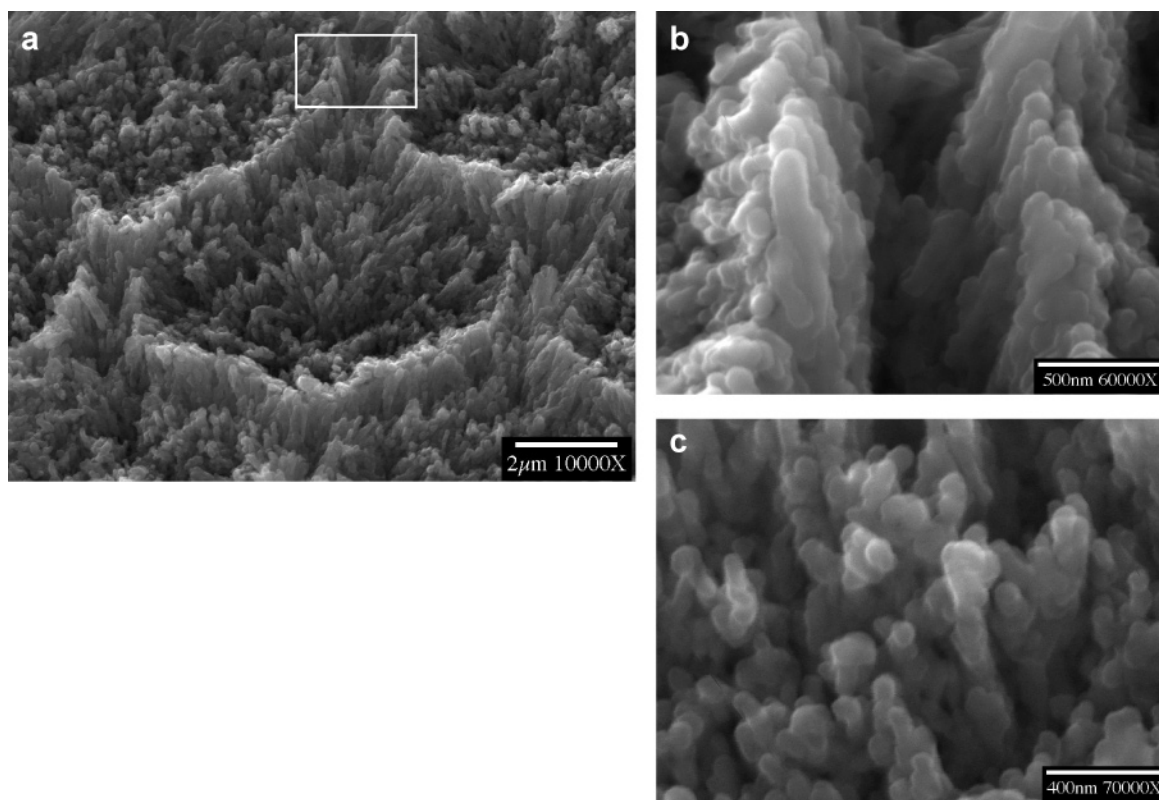

Figure 6. (a) Dissolution of wall and core (pH = 4.5, I = 0.15 mol L^{-1}, σ = 0.902, 37 °C). (b) Enlargement of the rectangular area of wall in (a). (c) Enlargement of core. Crystallites become smaller, and nanoparticles of apatite are formed on both walls and cores (dissolution time: 6000 min).

directly into the solution by fluid diffusion flux, resulting in empty cores (Figure 7). These particles were stable against dissolution in the bulk solution (Figure 8). Nanoparticles from walls also did not dissolve but adhered to the wall framework. High-magnification SEM confirmed that the remaining wall surfaces were covered by numerous small crystallites 100 ± 20 nm in size (Figure 9). All the results of in situ EDS, XRD, XPS, and IR studies indicated that these residual crystallites were apatitic phases similar to those prior to demineralization. The apatite particles, residues of the demineralization reaction,
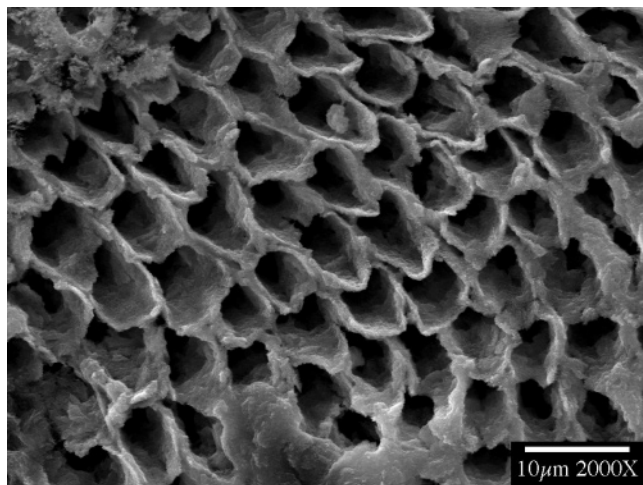
Nanoscale Enamel Dissolution

J. Phys. Chem. B, Vol. 109, No. 2, 2005 **1003**

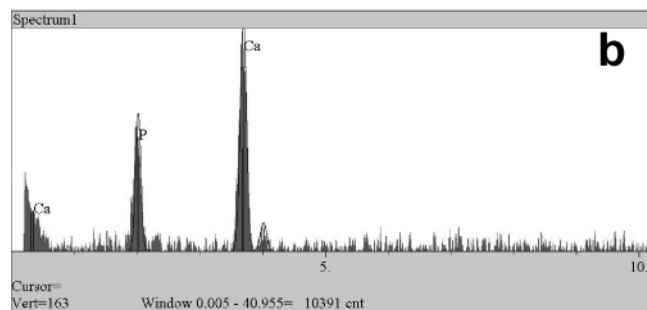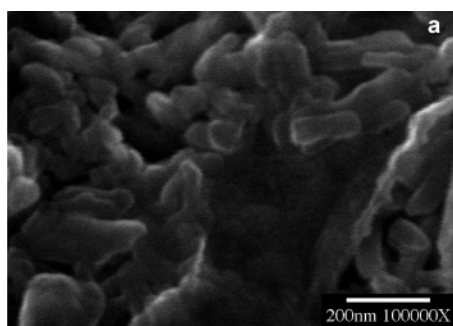**Figure 7.** SEM of hollow enamel cores after dissolution for 5 days.

Figure 8. (a) SEM of nanoparticles collected from the bulk solution by filtration at the end of a CC dissolution experiment; (b) EDS of nanoparticles.
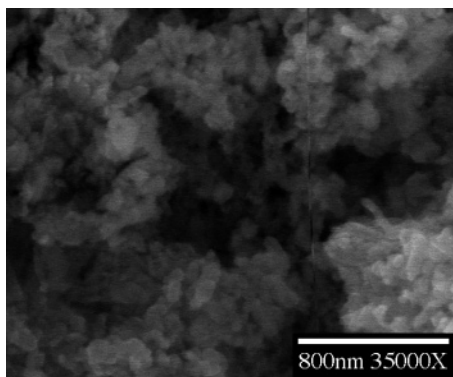

Figure 9. SEM of nanoparticle residues retained on wall surfaces.

Figure 10. CC curve. Plot of titrant volume against time for enamel dissolution (6 surfaces exposed to acid). The rate decreased virtually to zero after long reaction times.

from both wall and core dissolution, had the same size distribution range and were stabilized against further dissolution in the undersaturated aqueous solution. The CC dissolution curves reached plateaus prior to complete dissolution (Figure 10), indicating the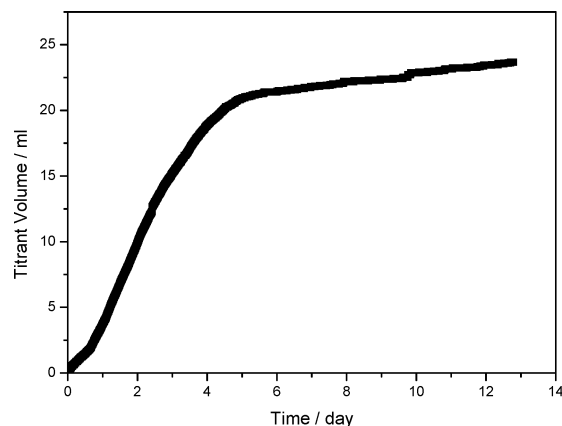 creation of metastable states in which the reaction was effectively suppressed even though the reaction solutions remained undersaturated. Mafe et al., who reported on this experimentally observed self-inhibiting dissolution of calcium hydroxyapatite (HAP),[25] suggested that it was due to the formation of a calcium-rich layer protecting the HAP surface. Fox et al. has quantitatively examined the phenomenon of metastable equilibrium solubility (MES) in synthetic and biological apatites.[26,27]

It is well-known that the dissolution of crystals is highly dependent on the thermodynamic driving forces, usually expressed in terms of the undersaturation, S, Hitherto, it was considered that, when $S < 1$, all crystals would inexorably dissolve until all the solid phases had disappeared. The demonstrated importance of pit formation during dissolution has markedly changed our understanding of this process. These pits provide dissolution sites, and the entire reaction proceeds by the formation and growth of pits.

In most kinetic studies, the dissolution rate R has been simply expressed by a rate law such as eq 4

$$R = k\sigma^n \tag{4}$$

where k is the rate constant, n is the effective reaction order ($n = 1$ for diffusion control), and σ is the relative undersaturation. Equation 4 implies that the dissolution rate, and thereby the dissolution step displacements, should remain constant at sustained undersaturation. However, recent CC studies of the dissolution of the calcium phosphates have shown that the rates decrease markedly with time despite a sustained undersaturation.[28,29] In some experiments, the rates approached zero even though crystals remained in the undersaturated solutions. It was shown that the surface-controlled crystal growth and dissolution is dominated by the movement of steps and by two conceptual mechanisms: the nucleation of stable clusters and the spiral-generating Burton–Cabrera–Frank (BCF) theory.[30] With the use of AFM and related technologies, many studies have described the presence of steps in a wide range of materials and monitored the motion of these steps during dissolution and growth.[31–33] Lasaga and Luttge have used vertical scanning interferometry during dissolution, Monte Carlo simulations of etch pit formation, and empirical bulk dissolution rates to derive a dissolution rate law that is consistent with data for several minerals. This rate law predicts that the slower rates of dissolution measured in the field arise from metastable phases that hinder the reactions and that the process is nonlinear even as equilibrium conditions are approached.[34]

In many crystal dissolution studies, the conditions are often far from equilibrium, and treatment of crystal dissolution data is made in terms of linear relations between rate and deviation from equilibrium. The most often invoked relation has been based on the principle of detailed balancing or transition-state theory leading to the rate law[33−35] expressed as eq 5

$$\text{Rate} = A(1 - e^{\alpha(\Delta G/RT)}) \qquad (5)$$

where A and α are general constants, dependent on pH, temperature T, or inhibitor molecules. ΔG (<0) is the Gibbs free energy of dissolution, and R is the gas constant. This equation most closely applies to the dissolution of rough surfaces and conditions that are far from equilibrium. When the undersaturation exceeds some critical value (ΔG_{crit}), the strain field of a dislocation will open up the hollow core to form an etch pit.[36] This concept was also developed by Lasaga et al.[37] in their treatment of mineral dissolution. It follows that, beyond the critical undersaturation, a spiral dissolution model was not applicable.

Recently, AFM studies[14,15] have revealed the existence of critical conditions for dissolution pit/step formation and the dependence of dissolution rates upon pit/step sizes for sparingly soluble calcium phosphates. Because pit formation and growth are the principal elements of the dissolution process, the microscopic critical-size effects should be embodied in any macroscopic dissolution model under similar experimental conditions. The self-inhibiting effects observed in bulk dissolution using a CC method show that particle size must be taken into account in studies of demineralization where kinetics is greatly influenced by crystallite sizes.

These results can be explained in terms of a dissolution model incorporating particle size considerations, which has been confirmed by CC and in situ AFM experiments. Demineralization of sparingly soluble salts such as apatite is generally initiated and accompanied by the formation and development of pits on the crystal surfaces, and the dissolution rates are also determined by the pit densities and spreading velocities. Analogous to the formation of two-dimensional nuclei/hillocks for crystal growth, in dissolution, the rate of step movement from a pit of radius r can be obtained from treatments similar to the model of Burton, Cabrera, and Frank[38,39]

$$R(r) = R_\infty \left[1 - \frac{e^{(1-S)r^*/r-1}}{e^{1-S} - 1} \right]$$

$$\approx R_\infty \left(1 - \frac{r^*}{r} \right) \qquad (6)$$

where r^*, the critical radius for the formation of a two-dimensional pit/dissolution step, is given by eq 7

$$r^* = \frac{\gamma_{SL}\Omega}{|\Delta g|} \text{ and } \Delta g = kT \ln S \qquad (7)$$

In eq 7, γ_{SL} is interfacial tension, k the Boltzmann constant, Ω the area occupied by each dissolution unit, and Δg the Gibb's free energy change for dissolution. In eq 6, R_∞ is the velocity of dissolution steps at $r \rightarrow \infty$. It has been shown that only pits which are larger than r^* provide the active dissolution sites that contribute to dissolution. When r is closer to r^*, there is no fast movement of its stepwave, and the dissolution rate approaches zero. When the dimensions of the crystallites (l's) fall into the same order as r^* during the dissolution (e.g., l becomes less than 20 r^*), the formation of active pits is more difficult, because their sizes are restricted to those of the small

crystallites. As shown by eq 6, $R(r)$ is strongly dependent on pit size. Correspondingly, the macroscopic CC dissolution rate decreases with the extent of dissolution. These small crystallites are difficult to detect when their sizes approach the critical value, r^*. Theoretical predictions are consistent with the CC dissolution results; for crystallite sizes approaching the critical values, the rates (slopes of the CC curves in Figure 10) decrease markedly with time despite the sustained driving force. Using an apatite interfacial tension, $\gamma_{SL} \approx 105$ mJ m^{-2},[40,41] and unit-cell dimensions $a = b = 9.432$ Å and $c = 6.881$ Å,[42] we estimate the value of r^* from eq 7 to be about 20−50 nm under these dissolution conditions. It is significant that the collected residues following apatite dissolution have similar size distributions (Figure 8). The formation of etch pits at the nanometer scale during crystal dissolution has also been suggested by other workers.[43−46] The model for enamel presented here is based on previous SEM and in situ AFM studies of synthetic calcium phosphates.[14,15,28]

To exclude the influence of complicating biological factors such as the possible presence of organic matrix components, CC dissolution studies have also been made using synthetic hydroxyapatite samples of high purity of ($>99.4\%$) with the same needlelike morphology as natural enamel. Similar reproducible self-inhibition dissolution behavior by nanosized crystallites was observed, dependent on undersaturation. Moreover, it has been suggested that the proteins (mainly amelogenins) that induce/control the crystallization of apatite are almost completely degraded or removed during enamel maturation.[47,48]

IV. Conclusions

Calcium apatite is the main constituent of many biological hard tissues such as dental inorganic tissues, and its chemical behavior forms a model for the study of important biological phenomena such as caries lesion formation. Therefore, the dissolution of synthetic calcium phosphates[49−51] or human enamel[52−56] in acid media has been extensively studied, but the proposed theoretical model is based on a phenomenological approach.

Generally, dissolution of minerals is regarded as a spontaneous reaction in which all the solid phase can be dissolved in undersaturated solutions. However, it has been found that demineralization reactions actually involve particle size dependent critical conditions of energetic control at the molecular level. This model is based on the movement of dissolution stepwaves stemming from pits/steps on surfaces. Only when pits are larger than the critical size do they contribute to the reactions, and the critical values are at the nanoscale level. One of the most important results is the strong nonlinear decrease in the rate until it approaches zero. The model is validated by extensive experimental data for the dissolution of sparingly soluble minerals such as the calcium phosphates. The decrease in the enamel dissolution rate has important implications for our understanding of caries lesion formation.

References and Notes

(1) Shore, R. C.; Robinson, C.; Kirkham, J.; Brookes, S. J. Structure of mature enamel. In *Dental Enamel: Formation to Destruction*; Robinson, C., Kirkham, J., Shore, R. C., Eds.; CRC Press: Boca Raton, FL, 1995.

(2) Ronnholm, E. *J. Ultrastruct. Res.* **1962**, *6*, 249−303.

(3) Cuisinier, F. J. G.; Steuer, P.; Senger, B.; Voegel, J. C.; Frank, R. M. *Cell Tissue Res.* **1993**, *273*, 175−182.

Nanoscale Enamel Dissolution

J. Phys. Chem. B, Vol. 109, No. 2, 2005 **1005**

(4) Cuisinier, F. J. G.; Steuer, P.; Senger, B.; Voegel, J. C.; Frank, R. M. *Calcif. Tissue Int.* **1992**, *51*, 259−268.

(5) Fincham, A. G.; Luo, W.; Moradian-Oldak, J.; Paine, M. L.; Snead, M. L.; Zeichner-David, M. Enamel biomineralization: the assembly and disassembly of the protein extracellular organic matrix. In *Development, Function and Evolution of Teeth*; Teaford, M. F., Meredith-Smith, M., Ferguson, M. W. J., Eds.; Cambridge University Press: Cambridge, 2000.

(6) Paine, M. L.; Snead, M. L. *J. Bone Miner. Res.* **1997**, *12*, 221−227.

(7) Fincham, A. G.; Moradian-Oldak, J.; Simmer, J. P. *J. Struct. Biol.* **1999**, *126*, 270−299.

(8) Kirkham, J.; Zhang, J.; Brookes, S. J. *J. Dent. Res.* **2000**, *79*, 1943−1947.

(9) Wen, H. B.; Moradian-Oldak, J.; Fincham, A. G. *Biomaterials* **1999**, *20*, 1717−1725.

(10) Wen, H. B.; Moradian-Oldak, J.; Fincham, A. G. *J. Dent. Res.* **2000**, *79*, 1902−1906.

(11) Robinson, C.; Kirkham, J.; Wearherell, J. A.; Richards, A.; Josephsen, K.; Fejerskov, O. *Caries Res.* **1988**, *22*, 321−326.

(12) Nikiforuk, G. *Understanding Dental Caries: Etiology and Mechanisms Basic and Clinical Aspects*; Karger: Basel, 1985.

(13) Gao, H.; Ji, B.; Ingomar, L. J.; Arz, E.; Fratzl, P. *Proc. Natl. Acad. Sci. U.S.A.* **2003**, *100*, 5597−5600.

(14) Tang, R.; Nancollas, G. H.; Orme, C. A. *J. Am. Chem. Soc.* **2001**, *123*, 5437−5443.

(15) Tang, R.; Orme, C. A.; Nancollas, G. H. *J. Phys. Chem. B* **2003**, *107*, 10653−10657.

(16) Tomson, M. B.; Nancollas, G. H. *Science* **1978**, *200*, 1059−1060.

(17) Anderson, P.; Elliott, J. C. *J. Dent. Res.* **1992**, *71*, 1473−1481.

(18) Anderson, P.; Elliott, J. C. *Caries Res.* **2000**, *34*, 33−40.

(19) Anderson, P.; Levinkind, M.; Elliott, J. C. *Arch. Oral Bio.* **1998**, *43*, 649−656.

(20) Gao, X. J.; Elliott, J. C.; Anderson, P. *J. Dent. Res.* **1993**, *72*, 923−930.

(21) Chow, L. C.; Takagi, S. *Caries Res.* **1989**, *23*, 129−134.

(22) Anderson, P.; Elliott, J. C.; Bose, U.; Jones, S. J. *Arch. Oral Biol.* **1996**, *41*, 281−290.

(23) Dowker, S. E. P.; Elliott, J. C.; Davis, G. R.; Wassif, H. S. *Caries Res.* **2003**, *37*, 237−245.

(24) Farina, M.; Schemmel, A.; Weissmuller, G.; Cruz, R.; Kachar, B.; Bisch, P. M. *J. Stuct. Biol.* **1999**, *125*, 39−49.

(25) Mafe, S.; Manzanares, J. A.; Reiss, H.; Thomann, J. M.; Gramain, P. *J. Phys. Chem.* **1992**, *96*, 861−866.

(26) Fox, J. L.; Yu, D.; Otsuka, M.; Higuchi, W. I.; Wong, J.; Powell, G. L. *J. Dent. Res.* **1992**, *71*, 1389−1398.

(27) Hsu, J.; Fox, J. L.; Higuchi, W. I.; Powell, G. L.; Otsuka, M.; Baig, A.; LeGeros, R. Z. *J. Colloid Interface Sci.* **1994**, *167*, 414−423.

(28) Tang, R.; Orme, C. A.; Nancollas, G. H. *ChemPhysChem* **2004**, *5*, 688−696.

(29) Tang, R.; Wu, W.; Hass, M.; Nancollas, G. H. *Langmuir* **2001**, *17*, 3480−3485.

(30) Lasaga, A. C. *Kinetic Theory in the Earth Sciences*; Princeton University Press: Princeton, 1998.

(31) Dove, P. V.; Hochella, M. F., Jr. *Geochim. Cosmochim. Acta* **1993**, *57*, 705−714.

(32) Dove, P. M.; Platt, F. M. *Chem. Geol.* **1996**, *127*, 331−338.

(33) Aagaard, P.; Helgeson, H. *Am. J. Sci.* **1982**, *282*, 237−285.

(34) Lasaga, A. C.; Luttge, A. *Science* **2001**, *291*, 2400−2404.

(35) Helgeson, H. C.; Murphy, W. M.; Aagaard, P. *Geochim. Cosmochim. Acta* **1984**, *48*, 2405−2432.

(36) Cabrera, N.; Levine, M. M.; Plaskett, J. S. *Phys. Rev.* **1954**, *96*, 1153−1156.

(37) Lasaga, A. C.; Blum, A. E. *Geochim. Cosmochim. Acta* **1986**, *50*, 2363−2379.

(38) Burton, W. K.; Cabrera, N.; Frank, F. C. *R. Soc. London Philos. Trans.* **1951**, *A243*, 299−358.

(39) Hartman, P. *Crystal growth: an introduction*; North-Holland: Amsterdam, 1975.

(40) Wu, W.; Nancollas, G. H. *Adv. Colloid Interface Sci.* **1999**, *79*, 229−279.

(41) Koutsopoulos, S.; Paschalakis, P. C.; Dalas, E. *Langmuir* **1994**, *10*, 2423−2426.

(42) Kay, M. I.; Young, R. A.; Posner, A. S. *Nature* **1964**, *204*, 1050−1052.

(43) Rufe, E.; Hochella, M. F., Jr. *Science* **1999**, *285*, 874−876.

(44) Jordan, G.; Higgins, S. R.; Eggleston, C. M.; Swapp, S. M.; Janney, D. E.; Knauss, K. G. *Geochim. Cosmochim. Acta* **1999**, *63*, 3183−3191.

(45) Luttge, A.; Winkler, U.; Lasaga, A. C. *Geochim. Cosmochim. Acta* **2003**, *67*, 1099−1116.

(46) Lasaga, A. C.; Luttge, A. *Eur. J. Mineral.* **2003**, *15*, 603−615.

(47) Teaford, M. F.; Smith, M. M.; Ferguson, M. W. J. *Development, Function and Evolution of Teeth*; Cambridge University Press: Cambridge, 2000.

(48) Pelton, A. R.; Gronsky, R.; Williams, D. B. *Images of Materials*; Oxford University Press: Oxford, 1991.

(49) Gramain, P.; Voegel, J. C.; Gumpper, M.; Thomann, J. M. *J. Colloid Interface Sci.* **1987**, *118*, 148−157.

(50) Thomann, J. M.; Voegel, J. C.; Gramain, P. *Calcif. Tissue Int.* **1990**, *46*, 121−129.

(51) Christoffersen, J.; Christoffersen, M. R.; Johansen, T. *J. Cryst. Growth* **1996**, *163*, 295−303.

(52) Margolis, H. C.; Zhang, Y. P.; Lee, C. Y.; Kent, R. L., Jr.; Moreno, E. C. *J. Dent. Res.* **1999**, *78*, 1326−1335.

(53) Higuchi, W. I.; Mir, N. A.; Patel, P. R.; Becker, J. W.; Hufferren, J. J. *J. Dent. Res.* **1969**, *48*, 396−409.

(54) Finke, M.; Jandt, K. D.; Parker, D. M. *J. Colloid Interface Sci.* **2000**, *232*, 156−164.

(55) Tanaka, M.; Kadoma, Y. *Caries Res.* **2000**, *34*, 241−245.

(56) Barbour, M. E.; Parker, D. M.; Allen, G. C.; Jandt, K. D. *Eur. J. Oral Sci.* **2003**, *111*, 258−262.